Adaptation for Climate Change

Design prototype of a high-resolution observation system based on novel plus conventional instrumentation

Deliverable Number 9.1

Status: draft version 1

Version: 1.0

Date: June 7th 2017

EC contract no 654110, HYDRALAB+

DOCUMENT INFORMATION

Title	Design prototype of a high-resolution observation system based on novel plus conventional instrumentation
Lead Authors	D. Hurther (CNRS-Grenoble), P.D. Thorne (NERC), F. Moulin (CNRS-Toulouse)
Contributors	J. Chauchat , G. Fromant , D. Hurther, T. Revil-Baudard, CNRS-Grenoble P.D. Thorne, NERC V. Dupuis, F.Y. Moulin, CNRS-Toulouse
Distribution	
Document Reference	

DOCUMENT HISTORY

Date	Revision	Prepared by	Organisation	Approved by	Status
May 18th 2017		D. Hurther	CNRS-Grenoble		
May 25th		P.D. Thorne	NERC		
June 6th		F.Y. Moulin	CNRS-Toulouse		

ACKNOWLEDGEMENT

The work described in this publication was supported by the European Community's Horizon 2020 Programme through the grant to the budget of the Integrated Infrastructure Initiative HYDRALAB+, Contract no. 654110.

DISCLAIMER

CONTENTS

1 DEVELOPMENT / IMPROVEMENTS OF ACOUSTIC CONCENTRATION & VELOCITY PROFILER TECHNOLOGY

1.1 CONTEXT & MOTIVATION

This part of Deliverable 9.1 of JRA COMPLEX is concerned with the improvement and optimization of the Acoustic Concentration & Velocity Profiler technology developped at CNRS-LEGI (Grenoble). The first prototype version has been designed within Hydralab IV-WISE as a flow measurement system capable of High-Resolution sediment Flux profiling across both the suspended sediment layer and the dense bedload layer. This unique measurement performance is based on the combination of the co-located and simultaneous measurement of the time-resolved sediment concentration, the 2C/3C particle-velocity field and the bed interfaces (bed level and lower suspension interface) across the entire bottom Boundary Layer generated under waves and / or currents. The ACVP technology integrates and implements the principles, technology and methodologies of multi-frequency Acoustic Backscattering Systems (ABS) with those implemented in Multi-bistatic pulse-to-pulse Coherent Doppler velocity profilers known as the ADVP technology. The spatio-temporal resolution is in the range of O(1mm) and O(10ms) to guaranty fine-scale studies of hydrodynamics and coupled sediment transport processes at small turbulent flow scales. Its deployment in Hydralab facilities such as wave channels, U-tubes or tilting open-channels was considered as a priority during the development phase so that its use in TA projects within hydralab+ (mainly in the CIEM-UPC and GWK-UH facilities) is possible. This guaranties unprecedented level of High-Resolution observations in the mobile sediment bed experiments of Hydralab+.

The experiments and measurement improvements during the first 18 months have focused on the validation and quantification of the acoustic sheet flow measurement performances. This point was identified as an essential lacking point at the end of Hydralab IV. For this purpose a detailed comparative analysis between the unique Conductivity Concentration Profiler technology (developed by J. Puleo at U. Delaware, USA) and the ACVP technology has been carried in the LEGI open-channel. The main results of this detailed comparative analysis is shown here

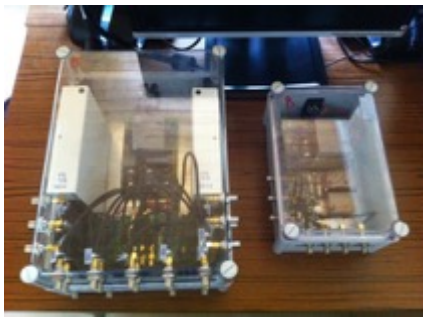
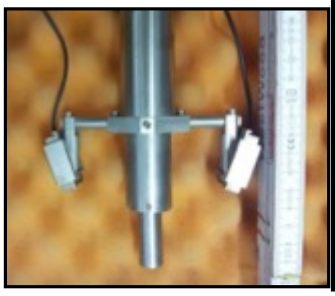


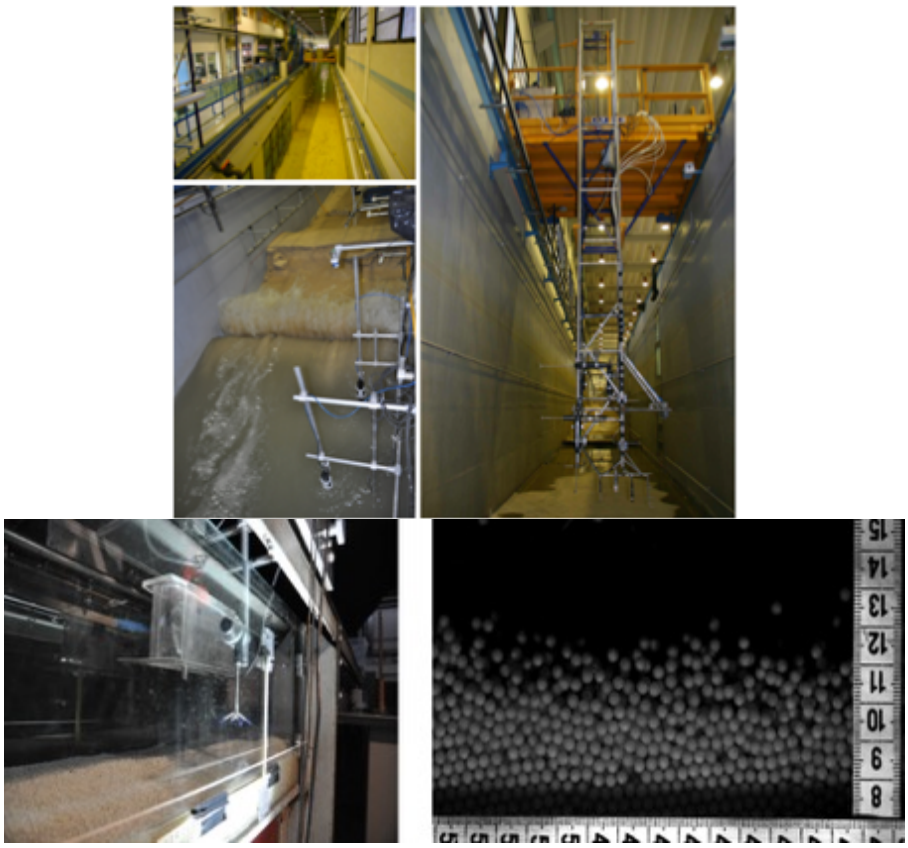

Picture 1 Electronic modules (Receivers and transmitter) of the Acoustic Concentration and Velocity Profiler (ACVP) with the new 1D2C sensor head (developed by CNRS-LEGI, D. Hurther, PA Barraud and J.-M. Barnoud). Deployment of ACVP and CCM+ technologies in UPC wave-channel.

1.2 EXPERIMENTAL SETUP AND FLOW CONDITIONS

The same experimental facility as in Revil-Baudard et al. [2015, 2016] was used to conduct the present experiment (figure 1). The LEGI/ENSE3 tilting flume is L = 10m long and W = 0.35 m wide with a tuning bed slope S0. A 3m long by 11cm high sediment reservoir is installed in the channel bed at 2m before the channel outlet.

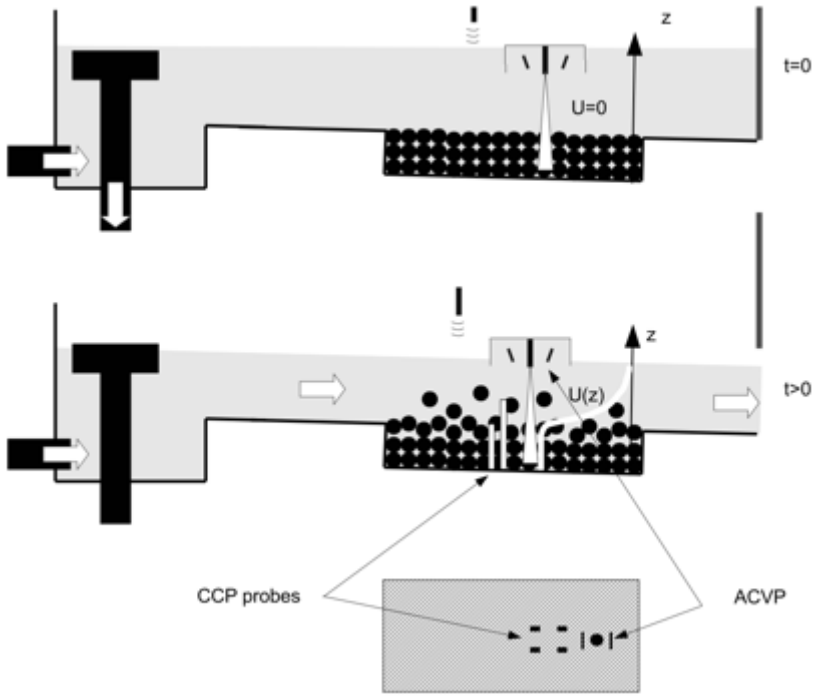

Figure 1 Sketch of the experimental facility and measurement protocol with flow instruments location.

The sediments used in this experiment are irregularly shaped PMMA particles (density ρp = 1192kg/m3) of median diameter dp = 3mm (further denoted as coarse ior large particles) and dp = 1mm (further denoted as fine or small particles). The particle size distribution is well-sorted, with a relative standard deviation (ratio of mean size to standard deviation of the suspended particles) σ0 = 0.015 for both particle diameters under the assumption of a log-normal particle size distribution. The mean settling velocity, ws = 5.5 cm/s and ws = 2.0 cm/s for coarse and fine particles respectively, has been measured experimentally from settling tests in a still water tank.

The flume is equipped with an acoustic limnimeter mounted on a moveable trolley for the measurement of the water level time series. These water level measurements are synchronized with the data acquisitions of the Acoustic and Concentration Velocity Profiler (ACVP). The flume was also equipped with the Conductivity Concentration Profilers (CCP) which is synchronized with the acoustic limnimeter as well. The four CCP probes were placed 8 cm upstream of the ACVP as shown in Figure 1. It must be noticed that the ACVP was not located at the vertical of the CCP probes to avoid undesirable acoustic echoes.

1.3 Results

In this section, time series of velocity, concentration and bed interface evaluated from both the ACVP and the CCP measurements are first shown for a single run. Then, the ensemble-averaged profiles of velocity, concentration, sediment flux and Reynolds shear stress are presented and

discussed. We finally focus on the comparison between the ACVP and CCP technology for concentration measurements.

1.3.1 Time series of velocity, concentration and bed interface

Figures 6 and 8 presents colorplot of velocity, concentration (ACVP), concentration (CCP) and the time series of the bed interface measured with the ACVP and detected from a criteria on the instantaneous concentration profile evaluated by the CCP.

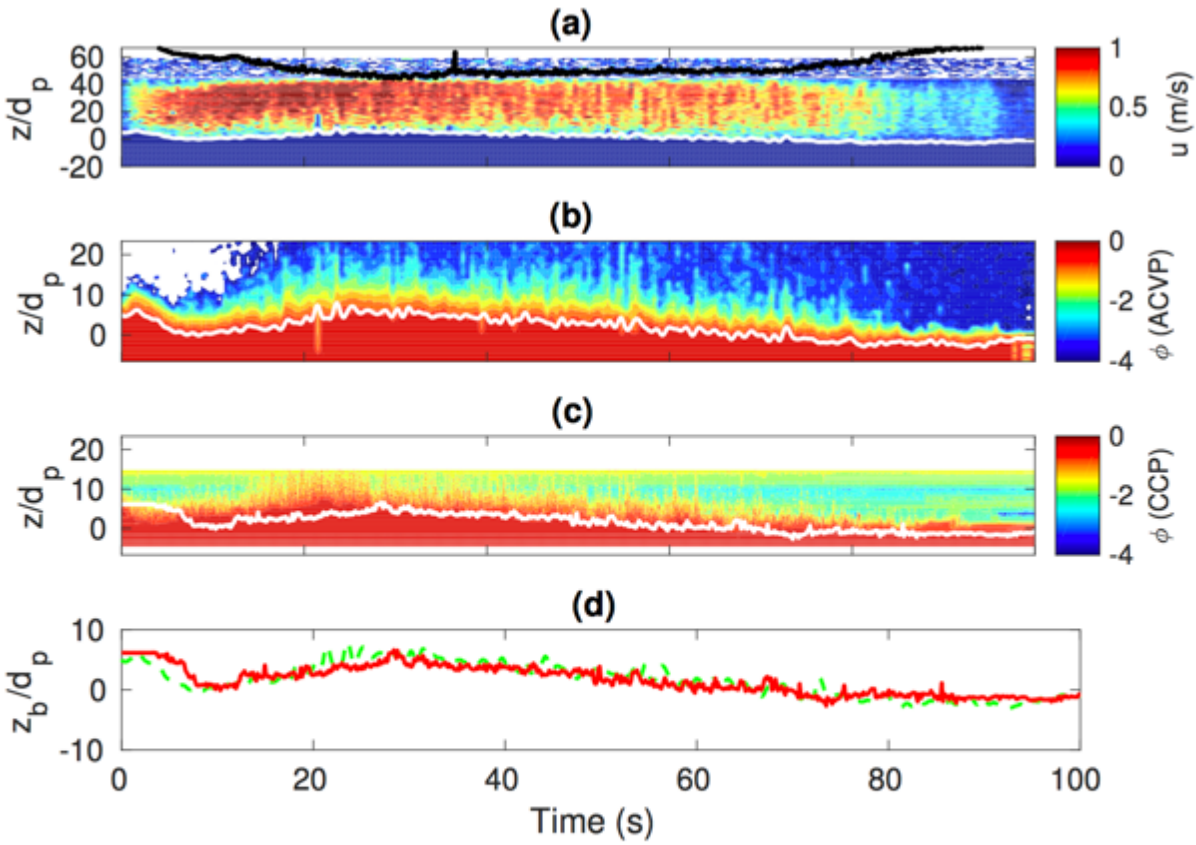

Figure 6. Colorplots of velocity, concentration (ACVP), concentration (CCP) and comparison between the ACVP and CCP bed interface detection (from top to bottom). One the first panel, the black line correspond to the water depth panel while the white ones correspond to the ACVP (ABIT method) and CCP bed interface detection. In the last panel ACVP bed interface detection is shown in green while the CCP one is shown in red.

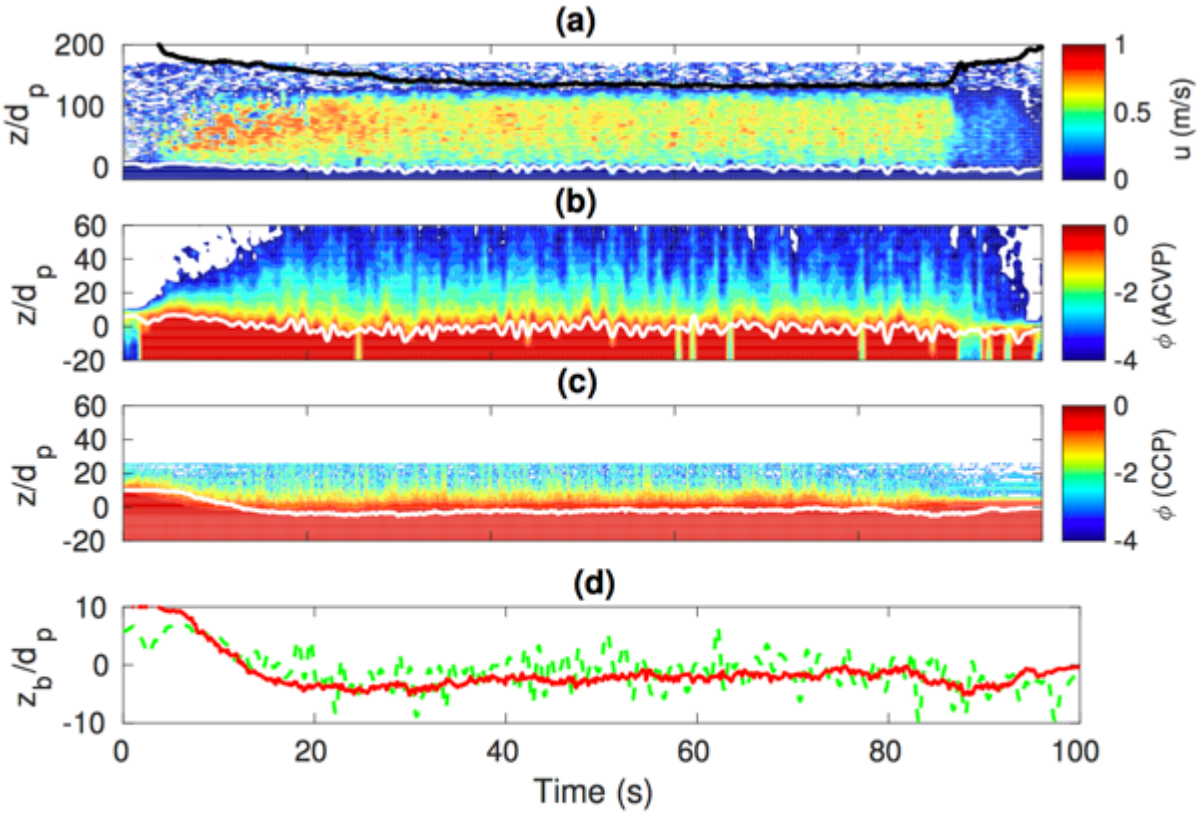

Figure 8. Colorplots of velocity, concentration (ACVP), concentration (CCP) and comparison between the ACVP and CCP bed interface detection (from top to bottom). One the first panel, the black line correspond to the water depth panel while the white ones correspond to the ACVP (ABIT method) and CCP bed interface detection. In the last panel ACVP bed interface detection is shown in green while the CCP one is shown in red.

A high velocity and high concentration time period is observed around t = 20 s. Afterwards, both quantities decrease with time. One must notice that the erosion rate (i.e. the drop of the bed interface with time) is stronger for the larger particles. The temporal derivative of the bed interface position zb is directly proportional to the spatial derivative of the sediment flux per unit width (Qs). It follows that the stronger erosion rate observed for the larger particles runs might be induced by a lack of sediment availability upstream of the measurement section. The small particles being easier to entrained in suspension upstream, it reduces the deficit in sediment supply and then also reduces the erosion rate observed for small particles runs.

A qualitative agreement is retrieved between the ACVP and CCP concentration measurement. It can be observed in figure 6b that bed interface is higher when the concentration is higher in the water column above. This result confirms the coupling between the bursting process and the bed dynamics highlighted by Revil-Baudard et al. [2015, 2016]; Liu et al. [2016].

It can be seen in figure 6d that the bed-interfaces detected by the ACVP and the CCP are in rather good agreement except that the the ACVP show larger intermittency for the fine particle case.

1.3.2 Ensemble averaged data

In order to enhance statistical convergence, the profiles of velocity, concentration, sediment flux and Reynolds shear stress are averaged over the N run realizations and over wide time windows (t ∈ [30 – 65] s for the large particles and t ∈ [40 – 80] s for the small particles). The obtained mean profiles are presented in figures 11 and 12 for the large and small particles, respectively.

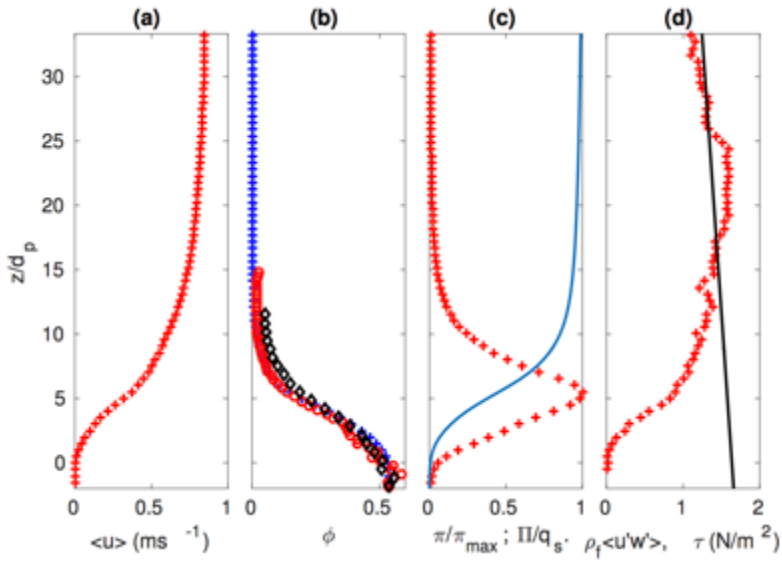

Figure 11. Ensemble and temporal average of velocity (a), concentration (b), sediment flux (c) and shear stress (d) for $SF04$ to $SF09$. In panel (b) the concentration has been measured by the ACVP (+) and the CCP (o, 1mm) and (diamounds, 2mm). The blue line in panel (c) corresponds to the cumulative flux (*i.e.* integrated from the bottom to the top) and the black line in panel (d) represent a linear fit of th shear stress profile.

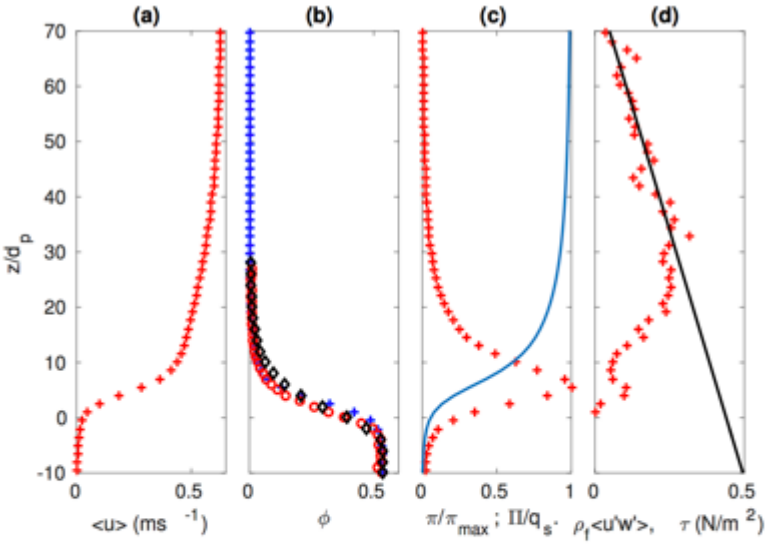

Figure 12. Ensemble and temporal average of velocity (a), concentration (b), sediment flux (c) and shear stress (d) for $SF16$, $SF17$ and $SF19$. In panel (b) the concentration has been measured by the ACVP (+) and the CCP (o, 1mm) and (diamounds, 2mm). The blue line in panel (c) corresponds to the cumulative flux (*i.e.* integrated from the bottom to the top) and the black line in panel (d) represent a linear fit of th shear stress profile.

The S-shape of the velocity profile already presented in Revil-Baudard et al. [2015, 2016] is retrieved in the present results. The concentration profiles are also similar than the ones presented previously. In the denser part of the flow (ϕ>0.1) the concentration decreases linearly with z whereas in diluted part (ϕ<0.1) a power law decay is observed. Both CCP and ACVP concentration measurements are in good agreement. The comparison between both datasets ise further analyzed in the following.

Concerning the sediment flux, it is interesting to notice that in both cases the flux is equally distributed between the suspension layer (ϕ<0.08) and the bed-load layer (ϕ>0.08) [Hsu et al., 2003]. The peak of sediment flux is also located close to the transition between the bed-load and the suspension layer. This result is consistent with value of the suspension number [S ≈ 1, Sumer et al., 1996]

The shear-stress profile shows that unlike the fine particle case, the flow is not frankly uniform and rather decelerated in the large particle case. The linear extrapolation of the shear stress represented by the solid line in figure 11d and 12d is used to compute the bed shear-stress at the position z = 0. This value is then used to evaluate the friction velocity, the suspension number and the Shields number (table 1). Different methods can be employed to evaluate the friction velocity. Even if the linear extrapolation is most probably the most accurate method for bed shear stress evaluation [van der A et al., 2011], one must keep in mind that it can be strongly affected by a misalignement of the ACVP relative to the mean flow direction [Peltier et al., 2013]. It leads to a relative uncertainty of about 20% on the friction velocity [Revil-Baudard et al., 2016].

1.3.3 Concentration measurements

Figures 13 and 14 present a zoom on the concentration profiles beside a semi-logarithmic representation. A very good agreement between the ACVP and CCP concentration measurements can be observed, especially in the range $\phi \in [0.01\ \phi\ 0.35]$. In the dense region, the ACVP predicts slightly larger concentration values than the CCP while in the diluted region the CCP predicts slightly higher concentration values. As the CCP is adapted to dense flow conditions and the ACVP to dilute flow conditions, one might conclude that the ACVP overestimates the mean concentration close to the dense regions (ϕ>0.35) while the CCP overestimates the concentration in the diluted regions (ϕ<0.01). These limits do not seem to depend on the sediment size. It might also depends on the sediment material properties.

One might argue that the overestimation of the ACVP concentration for ϕ 0.35 should lead to a wrong estimation of the total solid load during the experiment when compared with the topographic survey analysis. However, it is most probably compensated by an underestimation of the velocity in the associated regions due to the bed interface detection. It is well known that the minimum velocity predicted by acoustic profiler deployed over mobile sediment beds is different from zero. The ABIT method employed to detect the bed interface and to set velocity values to zero underneath allows to avoid an increase of velocity in the bed. However, it might set to zero velocity values which have in reality finite value. This underestimation of velocity together with the slight overestimation of concentration (figures (13 and 14) close to lower limit of the bedload layer might cancel each other out, leading to an appropriate sediment flux estimation as shown in Revil-Baudard et al. [2015] and figures (9 and 10).

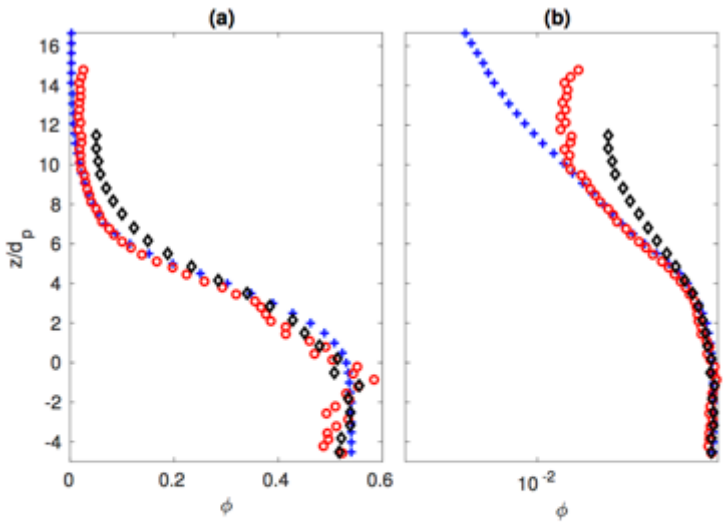

Figure 13. Comparison between ACVP (+) and CCP (o, 1mm) and (diamounds, 2mm) concentration measurements. The profile are presented with a logarithmic axis in panel (b) to highlight the suspension region. Panels (c) and (d) represent the RMS of concentration in linear and log axis respectively.

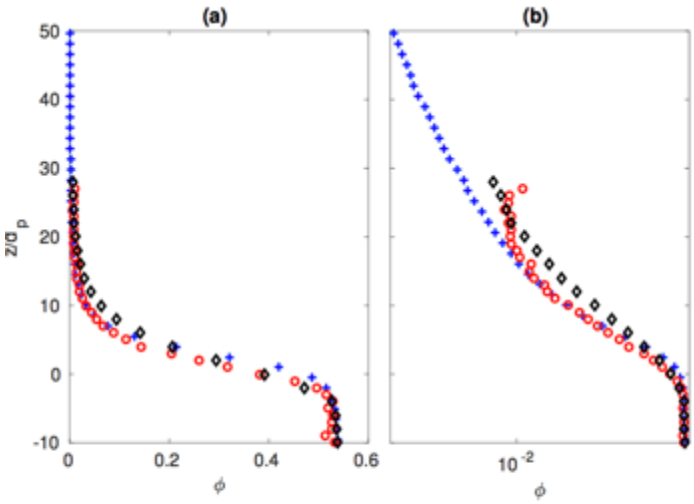

Figure 14. Comparison between ACVP (+) and CCP (o, 1mm) and (diamounds, 2mm) concentration measurements. The profile are presented with a logarithmic axis in panel (b) to highlight the suspension region. Panels (c) and (d) represent the RMS of concentration in linear and log axis respectively.

1.4 Conclusion

This comparative analysis between ACVP and CCP data in energetic particle sheet flows demonstrates the acoustic measurement capability of concentration profiles across the dense bedload layer. This extension of acoustic measurement performances opens new perspectives in process based sediment transport modelling, in particular for the development of new High-Resolution two-phase flow models applied to energetic flows. The present ACVP technology will be used in selected TA projects in order to improve the experimental measurement

2 Analysis of the 3D-ARP and BASSI for studies in COMPLEX

The complex interactions between bedforms, hydrodynamic and sediment mobility form the dynamic triad of sediment transport processes (Thorne and Hanes 2002). This triad is being increasingly probed by sophisticated measurement systems, to advance understanding and modelling of sediment transport. In this section, results from two recently developed systems for measuring bedforms and suspended sediments are presented. The two instruments are the 3-Dimensional Acoustic Ripple Profiler, 3D-ARP, and the Bedform And Suspended Sediment Imager, BASSI. The layout of the instrumentation for the study considered here is shown below in figure 15 and was carried out in the UPC wave flume facility, Barcelona. Measurements were collected for wave heights, H, between 0.3 m – 0.5 m and wave period, T=4.5 s.

Figure 15. a) Photograph of the instrumentation in the UPC wave flume showing the 3-Dimensional Acoustic Ripple Profiler, 3D-ARP, the Bedform And Suspended Sediment Imager, BASSI and the High Resolution Concentration and Velocity Profilers, HR-ACVP.

2.1 3-Dimensional Acoustic Ripple Profiler, 3D-ARP, measurements.

The 3D-ARP system is a self-contained battery powered autonomous dual axis mechanically scanning sonar underwater unit. The sonar has an oil-filled hemi-spherical plastic housing providing protection for its internally rotating transducer operating at 1.1 MHz with a narrow conical beam pattern. Typically, the sonar is mounted vertically, looking down at the bed, and captures a sequence of transects of the bed over a pre-programmed sector and range. The sonar gathers a single swath of data in the horizontal plane and then rotates the transducer through a pre-programmed angle around the vertical axis and repeats the process until a circular area underneath the sonar is scanned in a sequence of radial transects. The system is quite flexible and operates under software control; allowing operating range, pulse length, sampling interval, swath arc and rotation angles to be operator selected. The 3D-ARP also has a collection of sensors to measure conductivity, temperature, depth, pitch and roll; these are monitored for each dataset and stored in the data files. The profiles of the backscatter signal envelope are stored internally and post processed to extract the bed location to form transects along the bed that are combined to render a three dimension surface relief of the bed morphology.

In the study the 3D-ARP was mounted 1.0 m above the bed and operated by collecting a series of transects of the bed as the instrument rotated horizontally through 180° in 0.9° step intervals to build up high spatial resolution three dimensional measurements of the bedform morphology. Digitisation of the backscattered signal envelope was 1µs, thereby providing a radial range resolution in the millimetric regime. To illustrate the operation of the 3D-ARP, a transect from the instrument is shown in figure 16. It is seen in the figure that the interface between the bed and the water has been clearly identified as indicated by the white line and a representative transect of the bed obtained. The underlying slope was due to the 1/15 gradient of the bed and not due to the instrument. Two hundred such transects were obtained for each measurement.

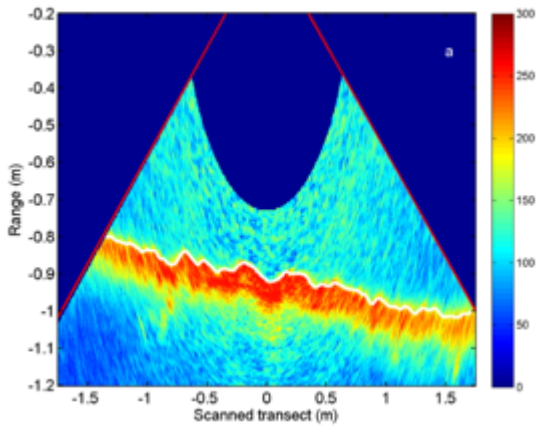

Figure 16. A single transect swath image of the backscattered signal from the 3D-ARP and identification of the bed echo indicated by the white line.

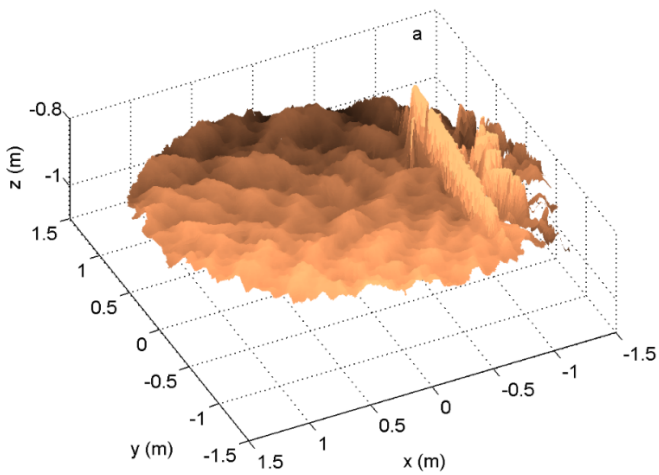

Figure 17. An image of the bed in the flume from the 3D-ARP for H=0.5 m, the vertical structure on the right hand side of the image is a reflection from the sidewall.

In figure 17 the bedform morphology constructed from the 200 profile transects is shown for the case of H=0.5 m. The vertical structure to the right hand side of the figure is a reflection from the sidewall of the flume, due to the mounting of the instrumentation not being centred in the flume. This image is typical of all the bedform measurements collected with the 3D-ARP and clearly shows that the bedforms were irregular and three dimensional in form. Such images as those shown in figure 17 illustrate the advantage of the 3D-ARP over a 2D-ARP, where it would not have been as straightforward to assess that the cross-flume variation in morphology was closer to three dimensional in nature, rather than two dimensional. As an independent check on the acoustic measurements, plan and side view photographs of the bed were collected and these observations were consistent with the scale and morphology of the bedforms measured acoustically.

To assess the consistency of the measured ripple dimensions with the 3D-ARP a number of repeat experiments were carried out at different wave heights. The results are shown in figure 18 for H=0.3 m, 0.4 m and 0.5 m. The results are seen to be consistent with the average ripple dimensions for 0.3 m having values of η=0.018±0.001 m, λ=0.22±0.018 m, η/λ=0.079±0.008, for 0.4 m of η=0.024±0.002 m, λ=0.29±0.018 m, η/λ=0.08±0.008 and for 0.5 m of η=0.039±0.005 m, λ=0.46±0.037 m, η/λ=0.084±0.012. The ratio of the standard deviation to the mean for the whole data set for σ(η)/ η, σ(λ)/ λ, and σ(η/λ)/(η/λ) respectively had values of 0.09, 0.08 and 0.1. Given that there will be some reconfiguration of the bed during the repeat experiments these result provide evidence for the repeatability of the 3D-ARP to accurately measure ripple dimensions.

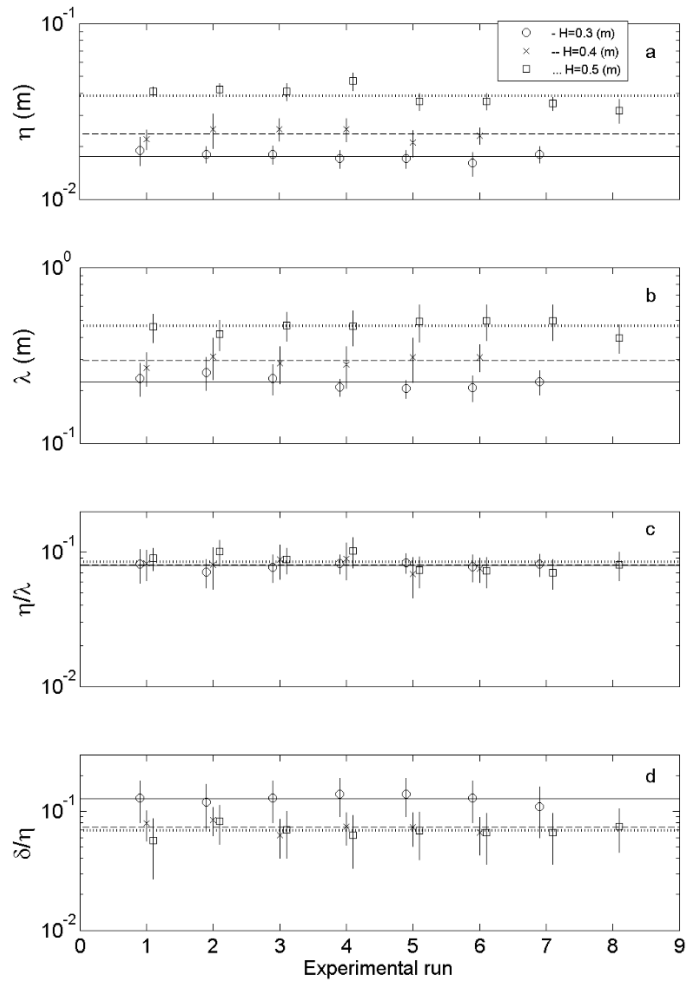

Figure 18. Measurements for repeated experimental runs at wave heights H=0.3, 0.4 and 0.5 m for ripple; a) height, b) wavelength, c) slope and d) the difference in heights between adjacent transects normalised by the mean ripple height for the experimental run. The lines represent a mean value for each value of H.

Another approach to look at consistency was to compare adjacent transects 0.9° apart. Given the decimetric horizontal scale of the bedforms, the expectation was that adjacent profiles would be very comparable. To carry out the analyse, the parameter δ⁄η was calculated, where δ= $\overline{|t_{hj} - t_{hi}|}$, t_h is the profile heights along a transect, subscripts i, j are adjacent transects and the over bar represents an average over all the transects for an experimental run. The results are shown in figure 18d. The mean values for δ⁄η over all experimental runs for H=0.3 m, 0.4 m and 0.5 m was

respectively 0.13, 0.07 and 0.07, which using the mean ripple heights for the three wave conditions yields a value for δ≈2 mm. Given that adjacent transect profiles are not identical this estimate is considered a reasonable estimate of repeatability and accuracy which is consistent with previous estimates (Bell et al 1998).

2.2 Bedform And Suspended Sediment Imager, BASSI.

The BASSI consisted of three transducer line arrays, each of which was connected to a common electronic scheduling unit that controlled the sampling parameters (Moate et al 2016). Each array contained 15 individual narrow beam disc transducers, consisting of five triple frequency groups 2.5 MHz, 1.25 MHz, and 0.75 MHz evenly spaced along the array. The transducer arrays were designed to be compact, being 0.5 m long, 0.14 m wide and 0.07 m in depth, to minimise interference with the measured sediment processes. Each array was self-contained, housing the transmit/receive electronics and data storage capacity. In the present study, the three transducer arrays (SN.001, SN.002, SN.003) were connected inline, and the complete system consisted of 45 transducers spaced regularly at 3.3 cm intervals over a 1.5 m range in the horizontal. To control the operation of the arrays a scheduling unit was used to provided flexibility in the instrument setup. This allowed a selection of options for the sampling range, the sampling interval, the pulse length, the number of profiles averaged over and the pulse repetition frequency.

When deploying the BASSI, only one group of three frequency adjacent transducers were operational at once in a given line array, with sequential advancement along the array to the next group of three frequencies. Hence, five transmit/receive cycles were required to sample across the whole array. Following data capture, the data were converted to 16 bit, averaged over a selected number of successive transmissions, and written to internal USB flash drives. When multiple transducer arrays were connected to the scheduling unit, as was the case here, the arrays electronically operated in parallel.

The main objective for developing the BASSI was to image suspended sediment structures over bedforms and thereby contribute to a better understanding of boundary layer sediment dynamics. In the first instance, an internal check was carried out to ascertain if the different frequencies yielded comparable concentrations. Figure 19 shows the near bed time varying suspended concentration field measured by three adjacent transducers of different frequency under regular waves of amplitude H=0.5 m and period T=4.5 s for array SN.001. As can be seen the temporal variations of the concentration are comparable in both magnitude and structure and the signature of a repeatable pattern due to the presence of regular wave as the main driving force is observed.

Following on from the comparison between individual transducers, the temporal variation in concentration was obtained by averaging over the 15 transducers in each array. The results for the three arrays are shown in figure 20 where again it can be seen that the magnitude, structures and repeatable pattern is observed. There are detailed differences in the suspended sediments between the arrays and these are likely associated with the three dimensionality of the bedforms and the location of the arrays relative to the bedforms.

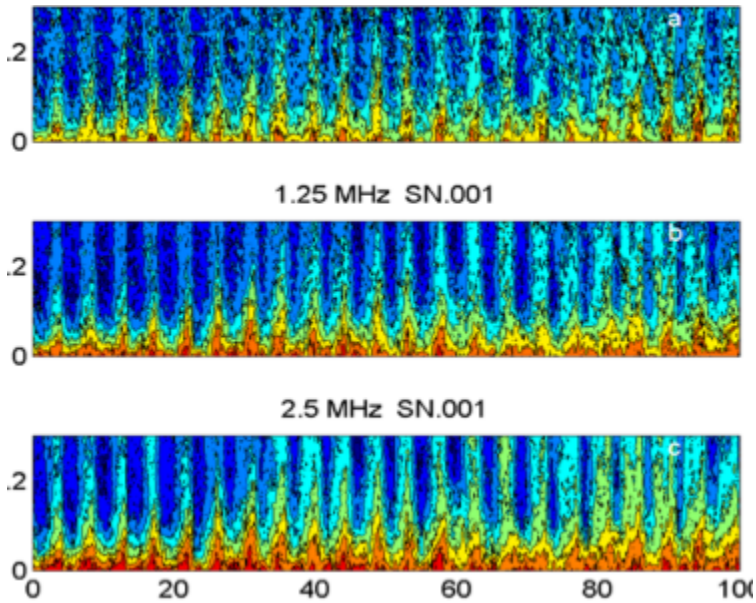

Figure 19. Time series of the suspended sediment concentration with height above the bed for array SN.001 measured at the three frequencies; a) 0.75 MHz, b) 1.25 MHz and c) 2.5 MHz.

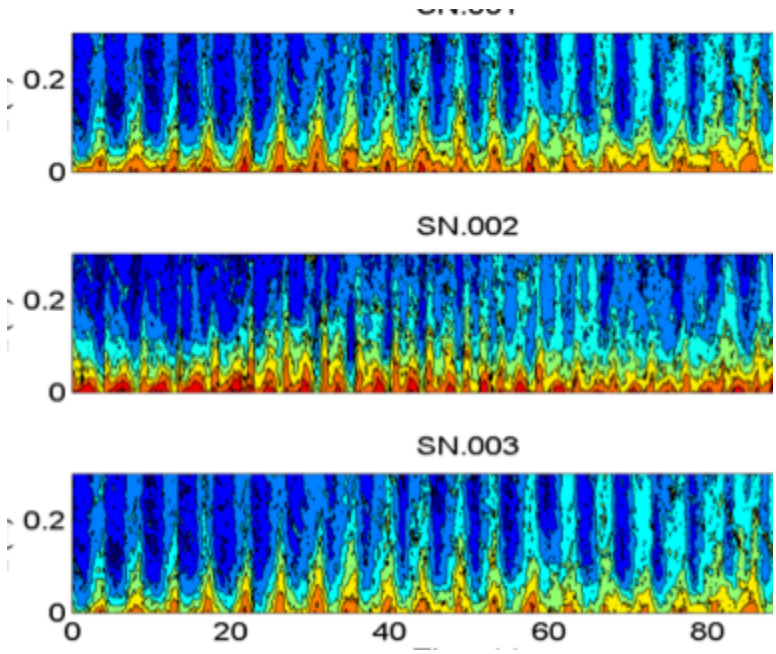

Figure 20. Time series of the suspended sediment concentration with height above the bed averaged across each array for; a) array SN.001, b) array SN.002 and c) array SN.003.

To provide direct quantitative comparison of the measured suspended sediments, concentrations profiles averaged over an experiment, which typically had a duration of 20 minutes, was calculated for each frequency for each array. The results are shown in figure 21 and it can be clearly seen that the near-bed concentration profiles are comparable for the three frequencies in each array and the magnitude and form of the suspended sediment profiles are consistent across the three arrays. The

results presented in figure 19-21 are indicative of the concentrations measured by the BASSI and support the capability of the instrument to obtain consistent concentrations over the three frequencies and across the 45 transducers that compose the BASSI.

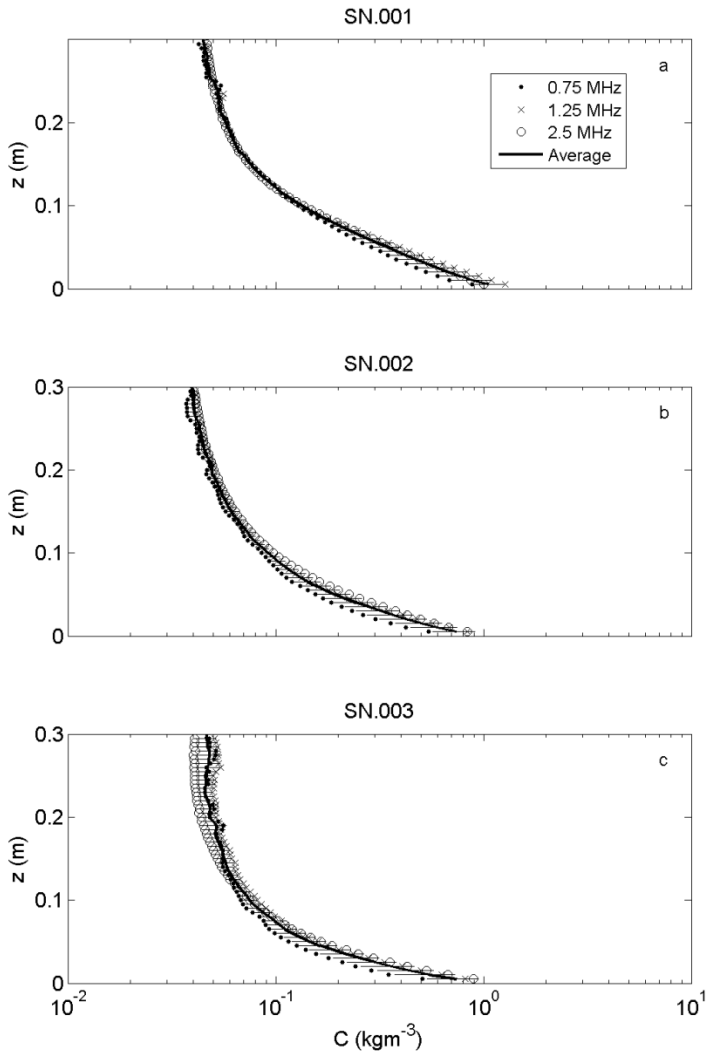

Figure 21. Mean suspended sediment concentration profiles averaged across an array and over the period of the experiment for; a) array SN.001, b) array SN.002 and c) array SN.003. The solid line with error bars is the average of the three frequencies.

Given the internal consistency of the BASSI analysis above, an example is presented in figure 22 of a two-dimensional vertical and horizontal, 2DHV, suspended sediment images generated by the BASSI. These shows a quasi-instantaneous (each recorded frame is a hardware average of 8 frames to reduce backscatter statistical configuration noise, Thorne and Hurther 2014) image of the bed and suspended sediments. The structure of the suspension is relatively complex due to the interactions of the wave hydrodynamics with the three dimensional bed. The images presented in figure 22 are a series of images 0.5 s apart are shown. It can be clearly seen in images 22a-22d that the main structures are moving from right to left in the figure, while in 22e-22h following flow reversal the structures in the image move from left to right. The images in figure 22 show the capability of the

BASSI to measure the time varying complex suspension field over a transect and therefore provides new opportunities for studying boundary layer sediment dynamics.

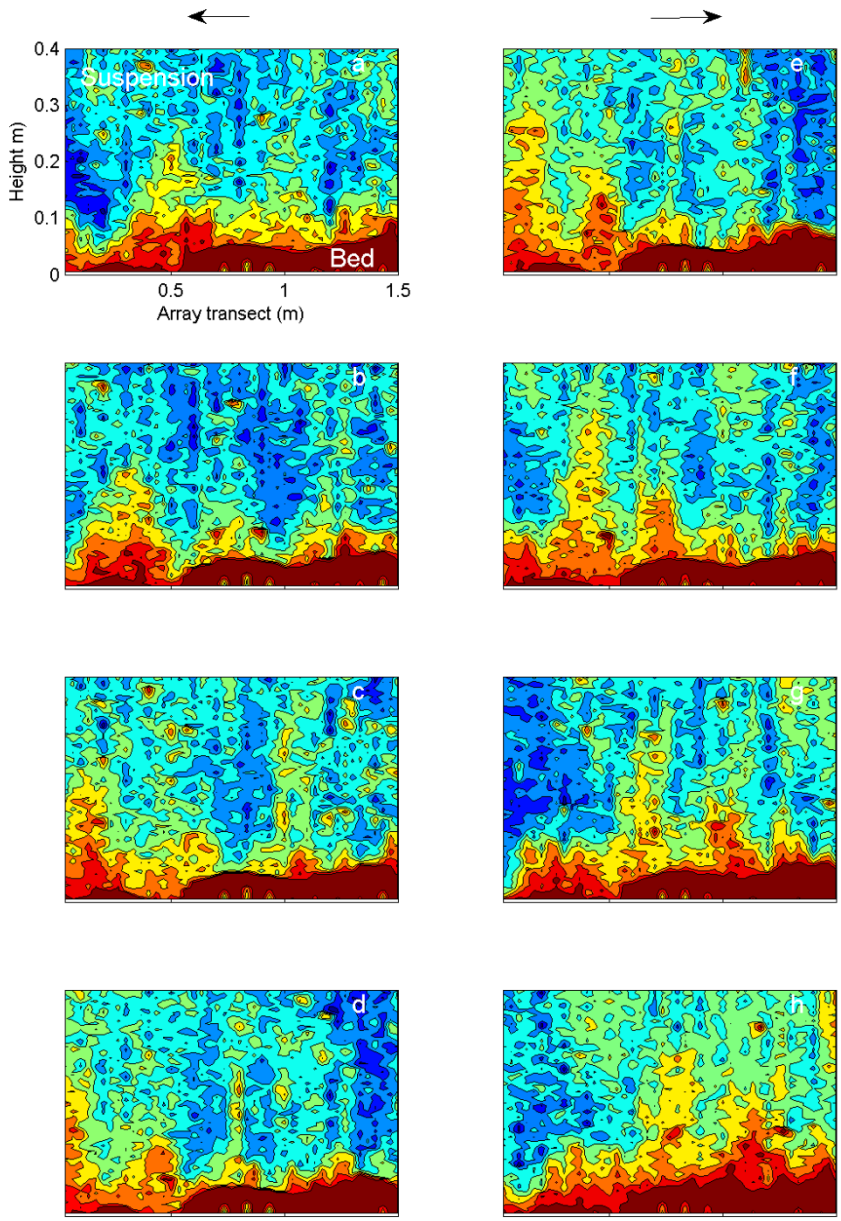

Figure 22. Sequential spatial measurements of the suspended sediment field at 2 Hz over 1.5 m during the passage of a wave over the BASSI. The arrows at the top of the panels indicate the direction of flow.

The BASSI was designed to obtain suspended sediments and bedforms over a transect. Therefore, over the 1.5 m cross-shore length of the BASSI the bed location was identified for each of the 45 transducers with a resolution of 0.005 m in the vertical and 0.033 m in the horizontal. As noted above the BASSI provided averaged profiles at 6 Hz and 40 of these 6 Hz profiles were averaged over to yield 0.15 Hz bedform transect measurements. Averaging over the 40 profiles improved the

robustness of the bed detection algorithm. A typical result is presented in figure 23a, which shows an intensity plot of the backscattered signal from the 45 transducers with a white line identifying the location of the bed. For this particular case H=0.4 m. In figure 23b is shown the evolution of the bedform transect over 1000 s and they are seen to be coherent over time. In figure 23c, the ripple dimensions over the 1000 s are presented and these are observed to be relatively uniform over the period.

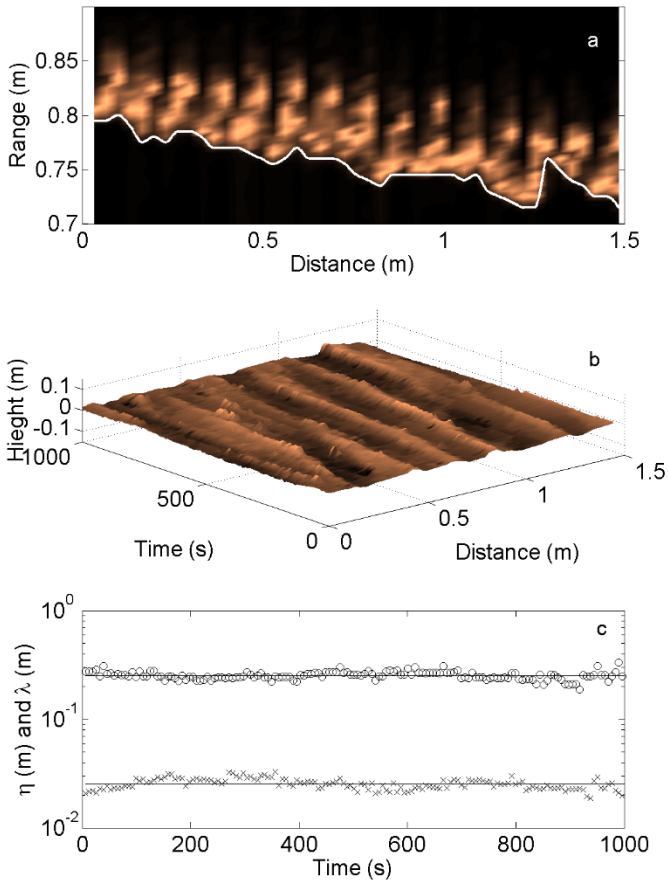

Figure 23. Measurements of bedforms from the BASSI during an experiment with H=0.4 m. a) A single transect image of the backscattered signal and identification of the bed echo indicated by the white line, b) evolution of a transect over time and c) variation of ripple height and wavelength with time with mean values given by the solid lines.

In figure 24, BASSI ripple dimensions from experiments repeated with the same wave height and period are presented, with the results being analogous to those in figure 18 from the 3D-ARP. Inspection of figures 18 and 24 show comparable ripple dimensions measured by both instruments. The average ripple dimensions from the BASSI for H=0.3 m had values of η=0.024±0.001 m, λ=0.24±0.02 m, η/λ=0.1±0.009, for H=0.4 m of η=0.029±0.0014 m, λ=0.27±0.03 m, η/λ=0.11±0.006 and for H=0.5 m of η=0.028±0.002 m, λ=0.4±0.06 m, η/λ=0.07±0.01. These results are very comparable with those from the 3D-ARP, though with the ripple heights showing some diverge.

Given that the 3D-ARP measurements were of a 3 m diameter area of the bed normally collected at the end of an experiment with the waves switched off, suspended sediment levels very low and the bed immobile, while the BASSI measurements were of a single cross-shore transect collected throughout an experiment with high levels of suspended sediment, it is not unexpected that the ripple dimensions from both instruments would not be identical, particularly with regard to the sensitive measurement of ripple height. It is therefore considered that the results from both instruments are consistent within their different methodologies of data collection.

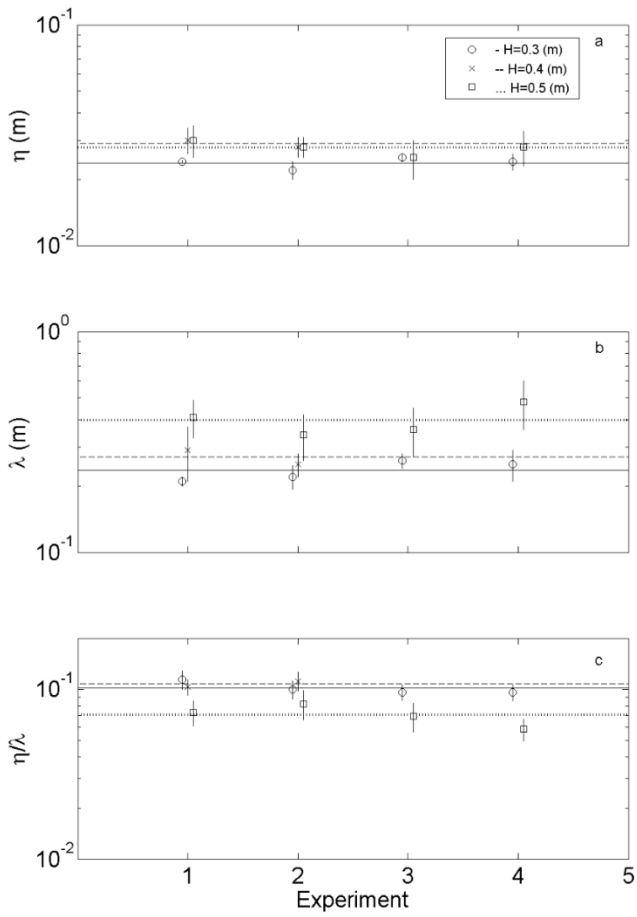

Figure 24 Measurements for repeated experimental runs at wave heights H=0.3 m, 0.4 m and 0.5 m for ripple; a) height, b) wavelength and c) slope. The lines represent a mean value for each value of H.

2.3 Discussions and conclusions

There is an ongoing requirement for instrument development to study near-bed boundary layer sediment transport processes. The complexity of the dynamics requires measurements at multiple temporal and spatial scales. The principle advantage of acoustics is that non-intrusive profiles of the bedforms, velocity and sediment mobility can be collected with systems which themselves can be mounted unobtrusively away from the near-bed processes under study, yet probe them downwards into the bed itself. Further, it is possible to obtain simultaneous collocated measurement of bedforms, flow and sediment mobility, allowing the dynamic interactions between these three components to be directly analysed.

To measure the morphology of the bedforms in the flume a 3D-ARP was deployed, this provides a series of horizontal transects over a selected swath and radially covering 180°, thereby allowing three-dimensional time varying measurements of the surface relief to be obtained. Measurement were collected under clear water and heavy suspended loads, of the order of several kgm^{-3} and transects of the bed morphology were readily obtained. The bedforms were strongly three dimensional, this was evident with the 3D-ARP, however, this would not have been readily identified with a 2D-ARP, which provides only a single transect. Experiments were repeated a number of times at three different wave heights and these have been used to assess the consistency of the measured bedforms. As shown in figures 18a-18d, repeatable values for ripple height, wavelength and slope were obtained with an indicative accuracy at the millimetre scale.

The BASSI was developed to study the interactions between the hydrodynamic, bedforms and sediment mobility, with a particular focus on bed features with decimetric wavelengths and centimetric heights, formed under the action of surface waves. To assess the internal consistency of the suspended sediment concentrations obtained with the system, time series and averaged vertical profiles were analysed at different frequencies and over the three arrays that composed the BASSI. The results shown in figures 19-21 illustrate the consistency of the results and support the veracity of the BASSI to measure a consistent suspension field across the transect measured by the arrays. To illustrate the time varying 2DHV capability of the BASSI a series of images of the bed and suspended field were presented in figure 22, where it can be clearly seen that suspended sediment structures could be tracked across adjacent images as a wave passed over the arrays. Measurements of bedforms were also made with the BASSI and the results were comparable with those obtained from the 3D-ARP.

3 3D-2C PIV MEASUREMENT TECHNIQUE FOR MULTI-SCALE TURBULENT FLOWS OVER NATURAL BEDS

3.1 CONTEXT & MOTIVATION

A major scientific challenge in helping to predicting the impact of climate change on natural systems is to be able to model the expected effects of changing wave and current regimes as well as extreme events. This implies modeling not only constant regimes but temporal changes at different time scales. To characterize the hydraulic forcing and interactions experimentally at the different time scales under conditions of high spatial variability (such as bed topology, plants, animals) the usual point, profile (e.g. acoustic) or even planar (e.g. PIV) measurement techniques are not adapted. The only way with current techniques to effectively characterize the usually turbulent flow field with transient hydraulic forcing is by phase averaging of a large number of experiments – very costly for larger-scale installation and not realizable with biological growth or morphodynamic evolutions. More complex random forcing even further increases the number of required experiments.

A significantly more cost-effective and also more easily interpretable solution is to measure the flow across the entire volume characteristic of the spatial heterogeneity at time scales faster than the smallest forcing time scale, i.e, instantaneously or quasi-instantaneously. Commercially available 3D measurement techniques such as tomographic methods are available, however, they are restricted in the size of the volume accessible (decimetric or in a slab), they suffer from relatively low spatial resolutions and are difficult to implement in large environmental hydraulic installations. Recent

developments at IMFT (Albagnac et al. 2013) based on a single high-speed camera and very rapid and micro-controlled scanning of the laser sheet have demonstrated the feasibility and advantages of a real 3D-3C (for 3 components) scanning measurement principle to resolve turbulent flows over a very wide range of scales, up to the metric scale. Temporally, the technique is fundamentally able to measure down to the turbulent micro-scale and can therefore be used to efficiently characterize all temporal and spatial scales up to the width of the flume. It has therefore the potential to measure effectively time-resolved instantaneous flows fields generated by extreme and transient forcings in volumes large enough to capture the spatial heterogeneity of the complex flows.

However, for measurements in hydraulic flumes over complex beds, the flow velocity is so high that a fully 3D-3C scanning technique is extremely difficult. As an intermediate step towards this technique, a 3D-2C (2 components measurement in a measurement volume) measurement technique was tested on a highly spatially heterogeneous turbulent flow: the flow in an hydraulic flume over a flow transverse variation of bed roughness. This bed configuration generates complex turbulence anisotropy induced 3D flow structures, with energetic secondary currents combined with an active horizontal mixing layer.

3.2 EXPERIMENTAL SET-UP

3.2.1 Flow generation

Experiments were carried out in a 26 m-long, 1.10 m-wide and 0.50 m-deep steep open-channel flume, with a slope of 0.3% and a 13.20 m-long working section made out of glass windows. The flume is located at the Institut de Mécanique des Fluides de Toulouse (IMFT). The water discharge ranges from 1 L/s up to 150 L/s. The flume works in a closed loop: the water is pumped from the downstream water tank and transported through closed pipes upstream into a 5 m long low-turbulence entry section. Within the entry section, the flow passes through a honeycomb and a series of mesh grids before converging at the main channel entry to establish inlet flow homogeneity and to reduce effects of both surface waves s and background turbulence.

In the downstream direction, the channel's glass bottom was fitted on the left half of the channel with a rough bed between x = 2.60 m and x = 24 m, where x is the longitudinal coordinate, the origin being defined at end of the entry section. The measurement area is located at x = 19.20 m. This left half rough bed was created by cubes of side h=4 cm arranged in a squared configuration with a frontal density (frontal area, A_f, to planar area, A_p) of λ_f=0.20. The right half of the flume was filled with smooth glass plates. The rough bed corresponds to the S1 configuration of the experiments discussed in Eiff et al. (2014). This setup was designed to trigger a strong horizontal mixing layer around the bed roughness discontinuity, and is schematized in figure 25.

Three relative submergence ratios D/h, where D is the water depth, equal to 2, 1.5 and 0.8 (emergent cubes) were studied.

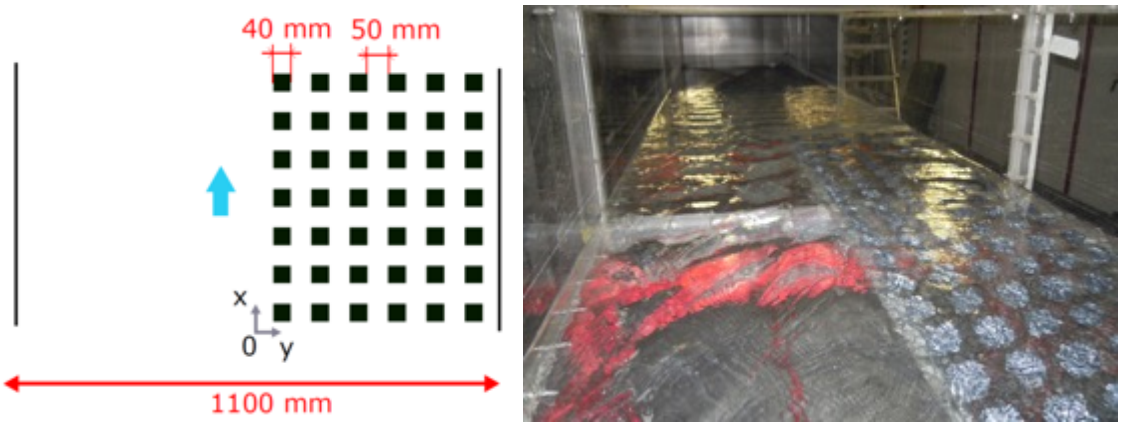

Figure 25 Sketch of the flume bed (left) and photograph of the flume (right) . Cubes of height h=4 cm are located on the left half of the flume. The right half of the flume remains smooth.

3.2.2 Optical measurements

A laser sheet is generated by a continuous laser (10W power) and a specific head that allows the generation of a 15 cm wide parallel laser sheet of 3 mm thickness. This laser sheet is reflected vertically by a 45° mirror placed on a motorized scanning system which allows high speed translation along a longitudinal axis. In the measurement region, high quality BK7 glass cubes were used in order to let the laser sheet cross them without shadow generation.

Images were recorded from the side with a high resolution (2048x2048) high speed camera (up to 1000 Hz), with high dynamics (14 bits). A telecentric lens was used in order to remove any parallax effects, yielding fields as large as 15 cm with a depth of field of around 30 cm.

The sketch of the experimental set-up is given in figure 26

The scanning velocity was chosen in order to get successive images with a certain amount of laser sheet overlap, but a maximal displacement of particles of around 15 pixels, which remains reasonable for PIV calculations. In these experiments, typical camera frequencies were around 700 Hz to achieve these conditions, with around 800 images for a scan along 20 cm depth with a 75% of overlap for the laser sheet.

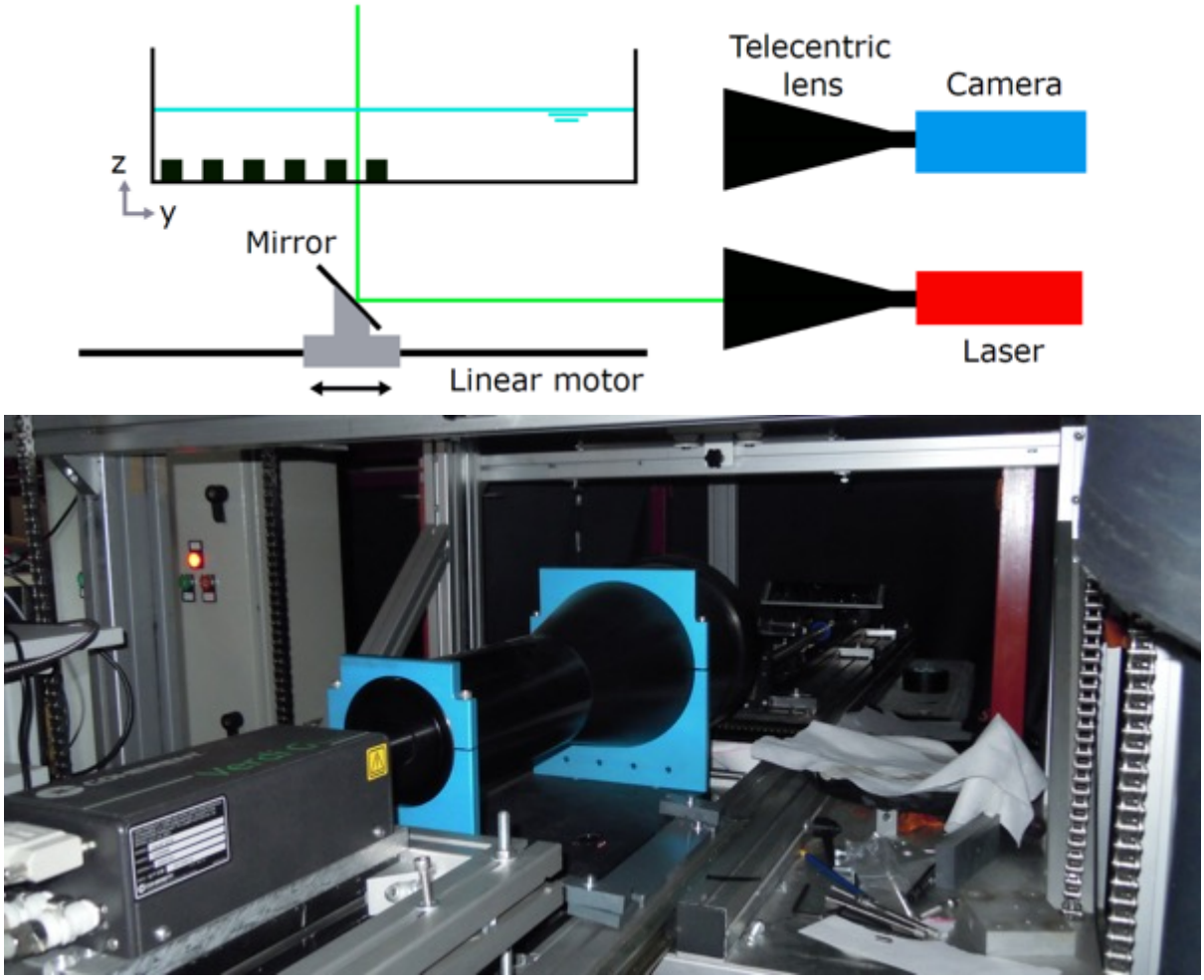

Figure 26 Sketch of the measurement technique (top) and photograph of the laser sheet generator and scanning motor (bottom).

3.3 VALIDATION AND RESULTS

3.3.1 Overlap

Essentially, as the laser sheet moves along the volume, successive images are acquired with an overlap ov defined as ov=(e-Δy)/e where e is the laser sheet thickness, Δy the displacement of the mirror between two successive images. The laser sheet thickness e is controlled optically. The displacement between two successive images Δy depends on the scanning velocity V and the camera frequency f. Since the camera frequency f is chosen in order to obtain a maximal displacement of 15 pixels between two successive images, the scanning velocity V is then prescribed by the formula V=fe(1-ov). The faster the scanning velocity, the smaller the overlapping between two successive images.

In figure 27, the percentage of false vectors in a scan near the interface (y=0) is plotted as a function of the overlapping ov between two successive images. Not surprisingly, the number of false vectors begins to increase dramatically for overlapping below 70%, in accordance with what is observed in classical 2D-2C PIV with pulsed laser when laser sheets from the two cavities are not perfectly aligned.

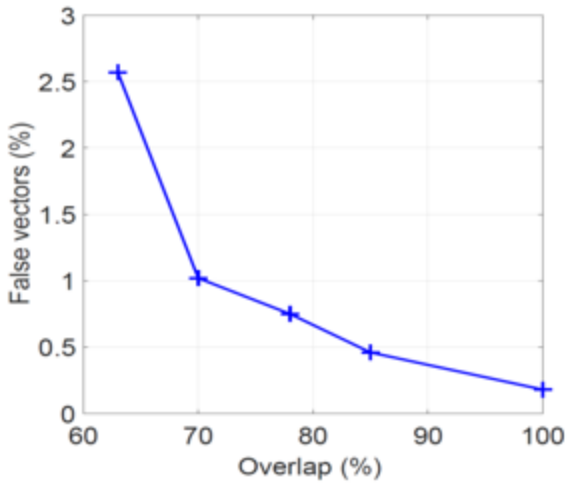

Figure 27 Amount of false vectors in scans with different levels of overlap.

3.3.2 Comparison with fixed 2D-2C velocity measurements

In the experiments, long acquisitions at fixed positions were also performed for comparison with the measurements during the scan. These fixed positions are noted Fix1 to Fix5. For the scans, due to limitations of the focused field of depth, different scans of around 25 cm of depth were performed in the flume, noted scan1 to scan4. The positions of the fixed planes and scans are plotted in figure 28.

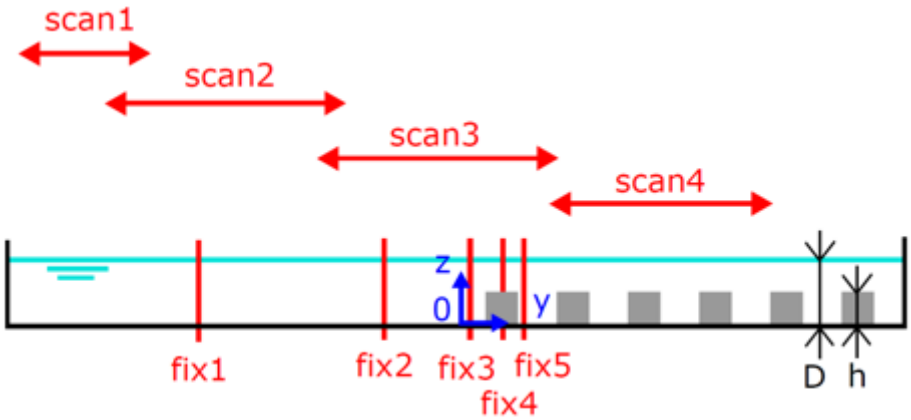

Figure 28 Positions of the fixed plane acquisitions and of the scans.

For the scans, due to the limited amount of camera memory, only 110 scans were acquired for each position (corresponding to around 80000 images). For fixed plane measurements, high frequency short acquisitions of about 10000 successive images were performed with the same frequency as for the scan, with individual acquisition durations of around 14s. Around 15 acquisitions were then performed for sufficient time convergence on the derived statistical moments, with a total duration of around 180s.

Since the scans were acquired every 2 s, the 110 scans can be considered as roughly statistical independent. In the second case, since the 10000 successive images were acquired at high frequency, they do not correspond to 10000 independent velocity measurements. However, since the total duration is around 180s, it corresponds roughly to 90 equivalent scans considering an integral time scales of around 3s, close to the 2 s interval between two successive scans.

In figure 29, vertical profiles of the longitudinal and vertical x-averaged velocity components are plotted at a specific lateral position, calculated with data of a fixed plane measurement and data of the plane in the corresponding scan. The overall behavior is well captured by the scanning system. The difference between the profiles is due to : 1) a lack of time convergence, with roughly 100 independent equivalent samples in the two cases, leading to a relatively high statistical biais error (proportional to rms/($N^{1/2}$) with N the number of independent samples) and 2) a better smoothing of short scale eddies in the fixed plane measurement due to the much higher number of PIV measurements (around 120000 velocity fields instead of 110).
Of course, it should be kept in mind that the scan gives access to measurements in 700 other plane and that in the figure 29, only one plane is discussed for comparison with the 2D-2C measurement technique.

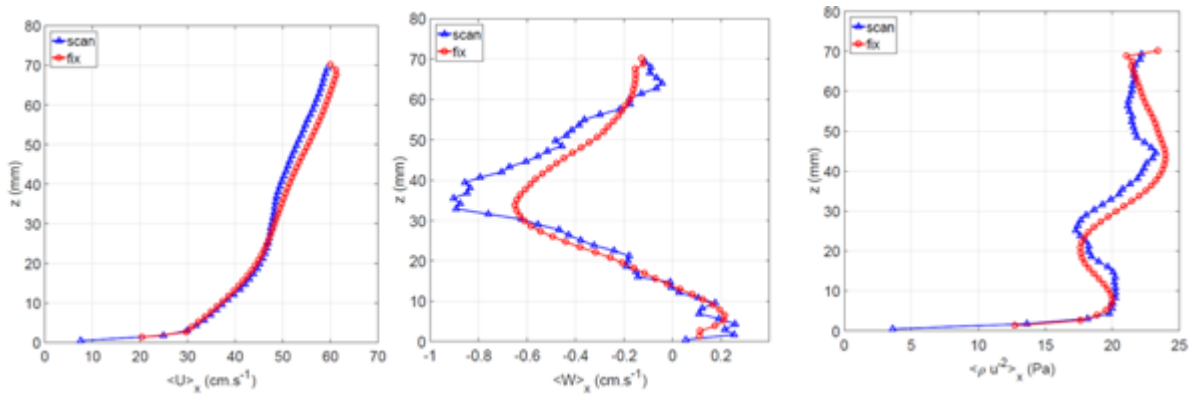

Figure 29 Vertical profiles at y=3 mm of x-averaged flow quantities inferred from fixed plane fix3 measurements and from scan3 measurements.

3.3.3 Statistics of the flow

The flow around the interface between the cube-filled part of the flume and the smooth part is highly three dimensional, even in terms of statistics.

When x-averaged in the longitudinal direction, the flow components measured by the scan give a very large view of the flow in a cross-section, as illustrated in figure 30 for the flow regime with D/h=2. The x-averaging operator is an averaging along one periodic pattern of cubes.

The flow quantities obtained with the scans can also give access to horizontal fields at different heights above or below the cubes, as illustrated by figures 31 and 32.

Of course, all these quantities, and especially the longitudinal velocity, can also be averaged in both time, longitudinal and vertical directions to have access to the transverse distribution of bulk velocity, as plotted in Figure 33, where the huge velocity difference between the smooth and the rough parts of the flume is striking.

This velocity difference, and more specifically the longitudinal velocity shear near the interface drives the growth of energetic horizontal mixing layer structures responsible for the increase of the turbulence there (see figure 30 near y=0).

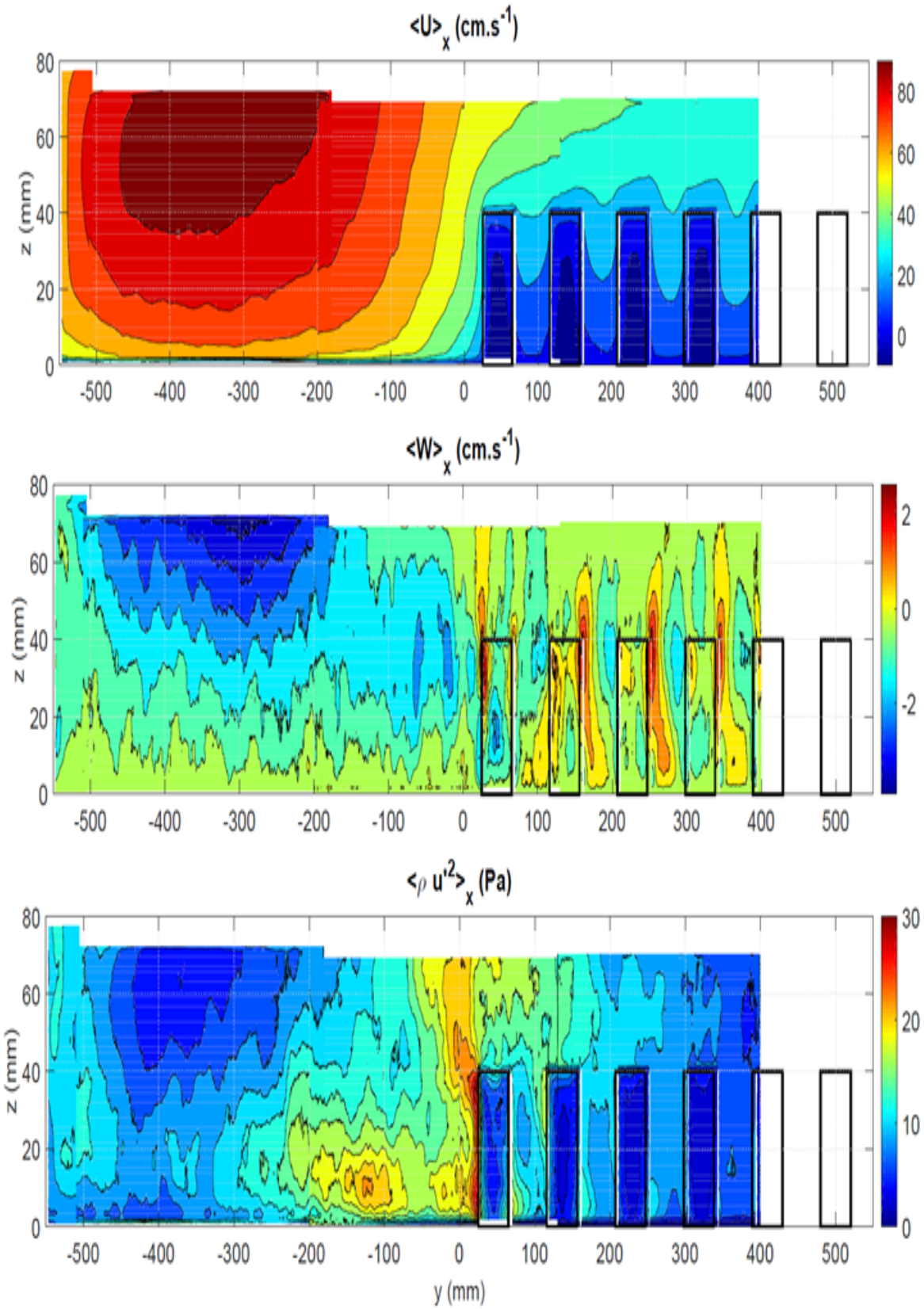

Figure 30 cross-section of x-averaged statistics, namely the x-averaged mean longitudinal and vertical velocities, and the longitudinal variance.

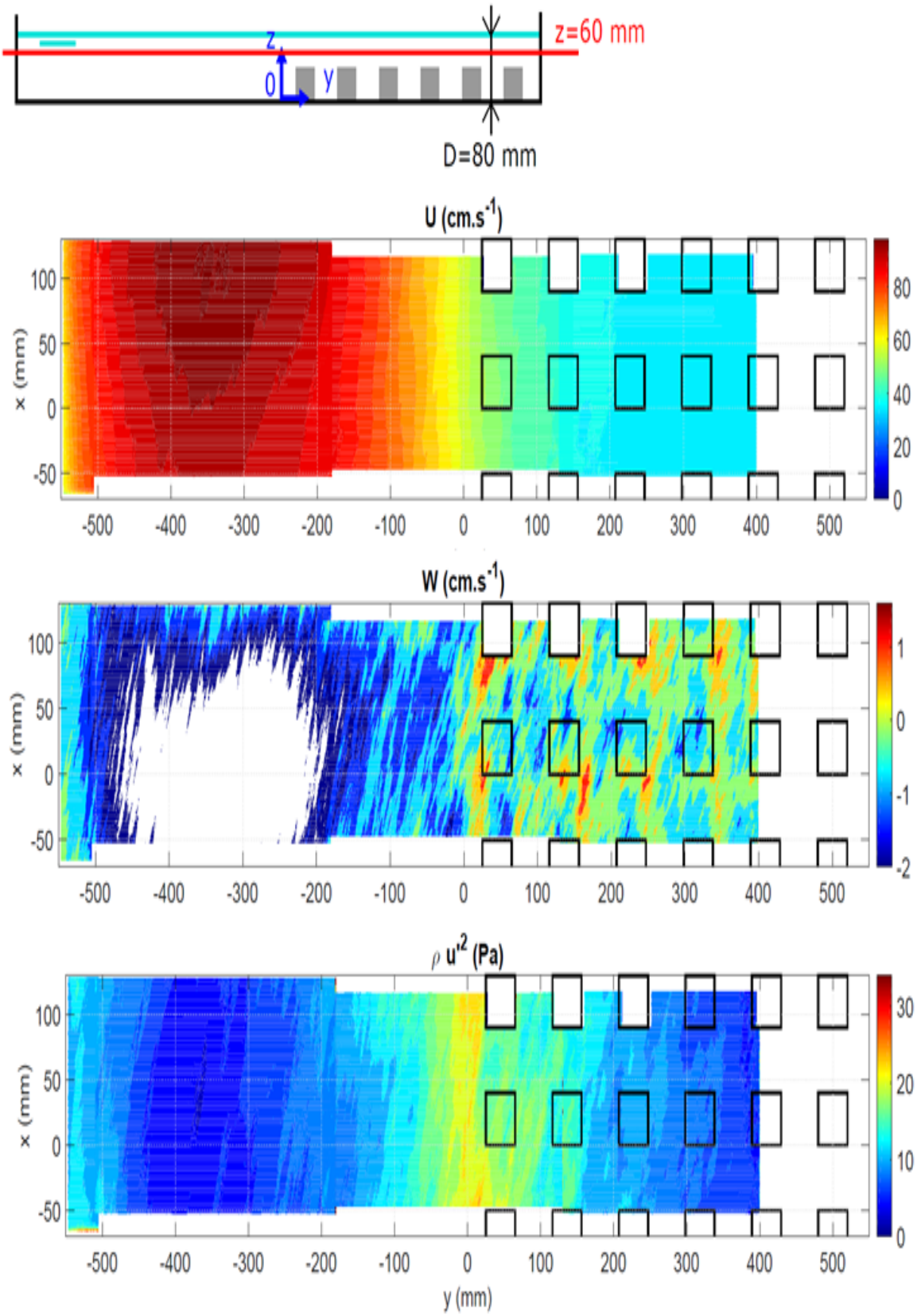

Figure 31 time-averaged statistics in an horizontal plane above the cubes, located at z=60 mm.

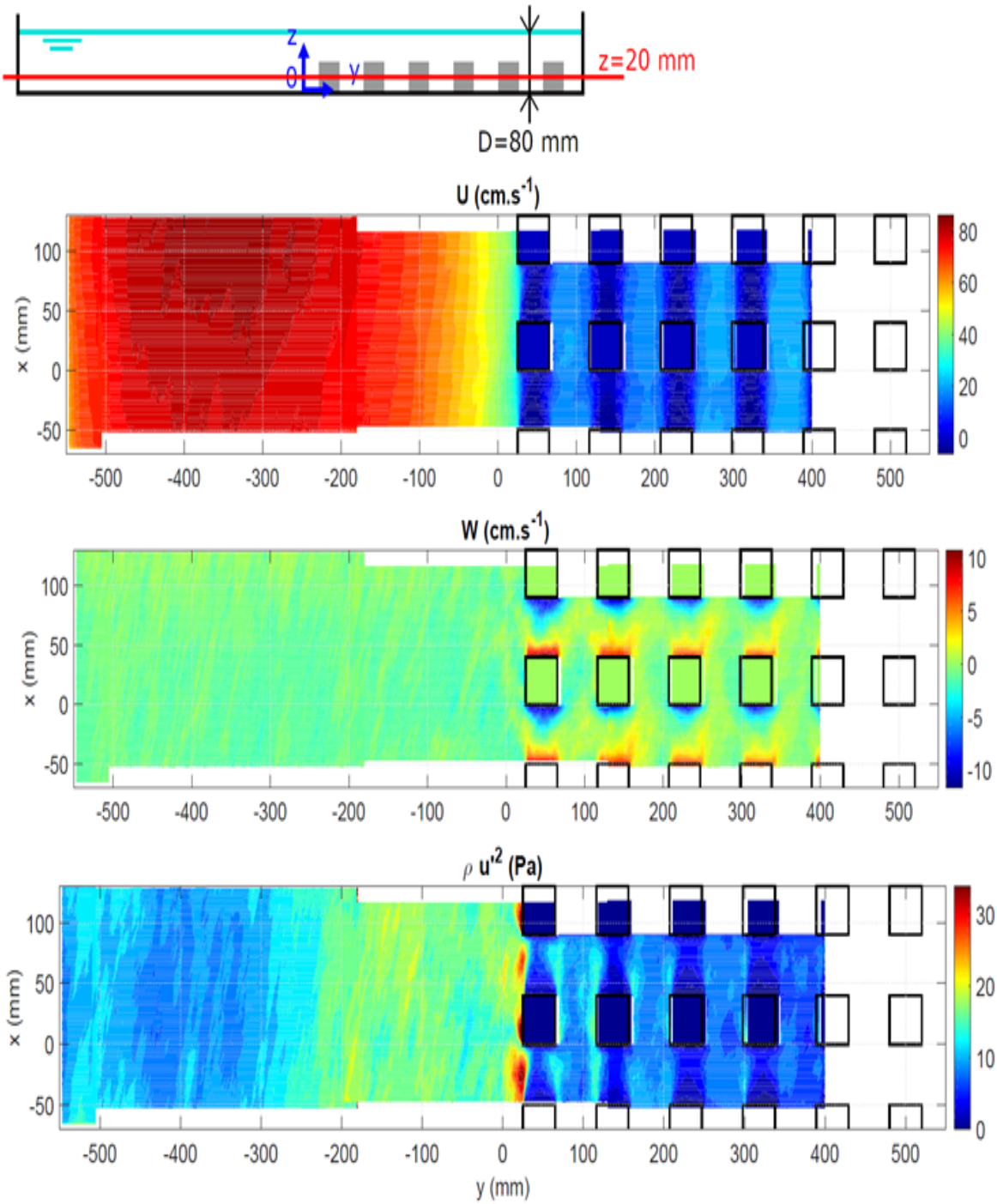

Figure 32 time-averaged statistics in an horizontal plane inside the canopy, located at z=20 mm.

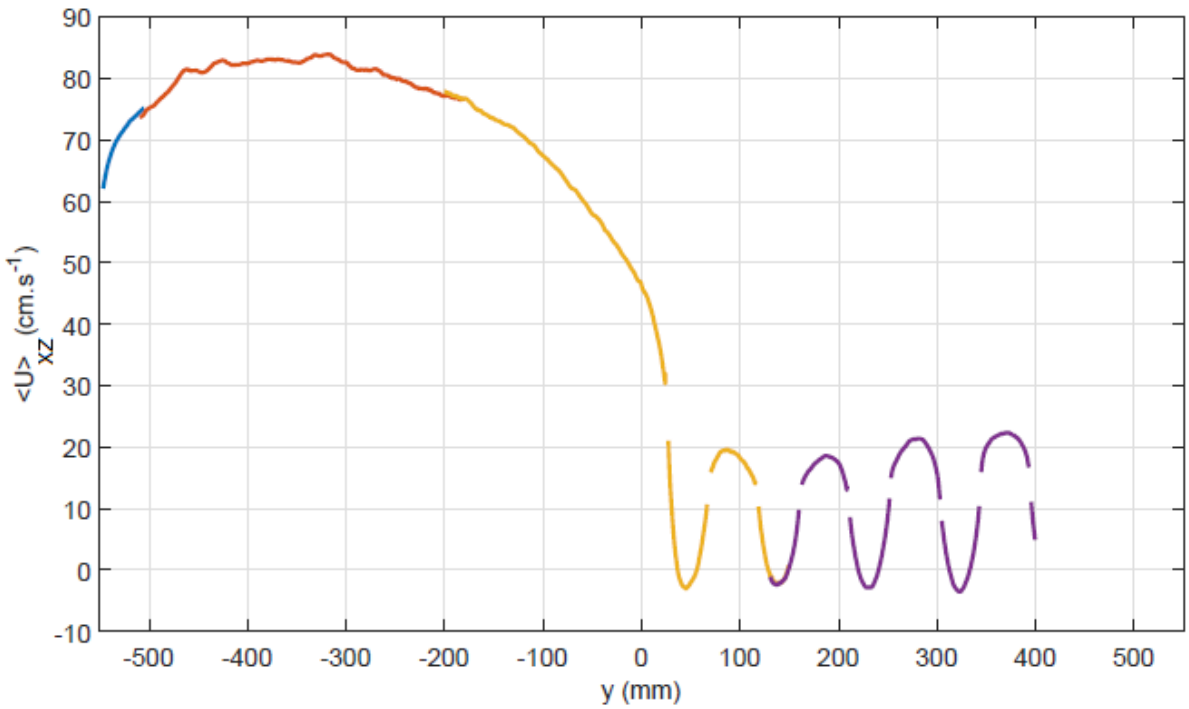

Figure 33 transverse profile of the bulk velocity obtained by time and spatial averaging along the longitudinal and vertical directions x and z.

3.4 Discussion and conclusion

The scanning 3D-2C PIV measurement technique gives access to the whole structure of this extremely complex flow. The main limitation was associated here to the use of a continuous laser and of a camera with limited memory and on-board grabbing system, which lead to time-convergence issues for the statistics. Yet, the flow structure description is far more complete and relevant for analysis than with point measurements (LDV, ADV) or fixed plane measurements (2D-2C PIV), which give only a partial view of the flow.

A promising improvement is the use of a double-pulsed high frequency laser instead of a continuous laser source. Beside the fact that the illumination of PIV particles will be better, it allows an independent set-up of the time step between the two images forming a burst (limited by the maximal displacement of 15 pixels) and the time step between two different planes during the scan. With less measurement planes (100 instead of 700 for exemple) by scan, the number of scans can be increased in order to achieve a better time convergence.

References

Albagnac J., Moulin F.Y., Eiff O., Lacaze L. and Brancher P. (2013), “A three-dimensional experimental investigation of the structure of the spanwise vortex formed by a shallow vortex dipole”, Environmental Fluid Mechanics, 14 pages, doi : 10.1007/s10652-013-9291-6

Bell, P.S., Thorne, P.D., Williams, J.J., 1998. Acoustic measurements of sand ripple profile evolution under controlled wave conditions. Proceedings of the fourth European Conference on Underwater Acoustics, held in Rome, Sept 21-25 1998 Vol.1, 353-358.

Berzi, D., Analytical Solution of Collisional Sheet Flows, Journal of Hydraulic Engineering, 137(10), 1200–1207, 2011.

Bricault, M., R´etrodiffusion acoustique par une suspension en milieu turbulent: application `a la mesure de profils de concen- tration pour l´´etude de processus hydros´edimentaires, Ph.D. thesis, Grenoble, INPG, 2006.

Chassagneux, F. X., and D. Hurther, Wave bottom bound- ary layer processes below irregular surfzone breaking waves with light-weight sheet flow particle transport, Journal of Geophysical Research: Oceans, 119 (3), 1668–1690, doi: 10.1002/2013JC009338, 2014.

Chiodi, F., P. Claudin, and B. Andreotti, A two-phase flow model of sediment transport: transition from bedload to sus- pended load, Journal of Fluid Mechanics, 755, 561–581, doi: 10.1017/jfm.2014.422, 2014.

Eiff, O., Florens, E . and F . Y . Moulin. ”Roughness parameters in shallow open-channel flows”, River flow 2014, 7th international conference on fluvial hydraulics, Lausanne, Swizerland. doi : 10.1201/b17133-44

Gaunaurd, G., and H. Uberall, Analysis of monostatic and bistatic acoustic echoes from an elastic sphere, The Journal of the Acoustical Society of America, 73(1), 1–12, 1983.

Hefner, B. T., and P. L. Marston, Backscattering enhancements associated with subsonic rayleigh waves on polymer spheres in water: Observation and modeling for acrylic spheres, The Journal of the Acoustical Society of America, 107(4), 1930– 1936, 2000.

Hsu, T., J. T. Jenkins, and L. F. Liu, On two-phase sediment transport: Dilute flow, J. Geophys. Res., 108, 14, 2003.

Hurther, D., and U. Lemmin, Shear stress statistics and wall similarity analysis in turbulent boundary layers using a high resolution 3D ADVP., Journal of Oceanic Engineering, 25, 446–457, 2001.

Hurther, D., and U. Lemmin, Improved Turbulence Profiling with Field-Adapted Acoustic Doppler Velocimeters Using a Bifre- quency Doppler Noise Suppression Method., Journal of Atmo- spheric and Oceanic Technology, 25, 452–463, 2008.

Hurther, D., P. D. Thorne, M. Bricault, U. Lemmin, and J. Barnoud, A multi-frequency Acoustic Concentration and Velocity Profiler (ACVP) for boundary layer measurements of fine-scale flow and sediment transport processes, Coastal En- gineering, 58, 594–605, doi:10.1016/j.coastaleng.2011.01.006, 2011.

Jackson, R., Locally averaged equations of motion for a mixture of identical spherical particles and a Newtonian fluid, Chemical Engineering Science, 52, 2457–2469, 1997.

Jenkins, J. T., and D. M. Hanes, Collisional sheet flows of sedi- ment driven by a turbulent fluid, Journal of Fluid Mechanics, 370, 29–52, doi:10.1017/S0022112098001840, 1998.

Lee, T. H., and D. M. Hanes, Direct inversion method to measure the concentration profile of suspended particles us- ing backscattered sound, Journal of Geophysical Research: Oceans, 100(C2), 2649–2657, 1995.

Liu, D., X. Liu, X. Fu, and G. Wang, Quantification of the bed load effects on turbulent open-channel flows, Journal of Geophysical Research: Earth Surface, 121(4), 767–789, doi: 10.1002/2015JF003723, 2015JF003723, 2016.

Moate, B. D., and P. D. Thorne, Scattering from suspended sedi-ments having different and mixed mineralogical compositions: Comparison of laboratory measurements and theoretical pre- dictions, The Journal of the Acoustical Society of America, 133(3), 1320–1334, 2013.

Moate B. D., Thorne P. D. and Cooke R. D. 2016. Field deployment and evaluation of a prototype autonomous two dimensional acoustic backscatter instrument: The Bedform And Suspended sediment Imager (BASSI). Continental Shelf Research 112 78-91

Peltier, Y., N. Rivire, S. Proust, E. Mignot, A. Paquier, and K. Shiono, Estimation of the error on the mean velocity and on the reynolds stress due to a misoriented {ADV} probe in the horizontal plane: Case of experiments in a compound open- channel, Flow Measurement and Instrumentation, 34, 34 – 41, doi:http://dx.doi.org/10.1016/j.flowmeasinst.2013.08.002, 2013.

Revil-Baudard, T., and J. Chauchat, A two-phase model for sheet flow regime based on dense granular flow rheology, Jour- nal of Geophysical Research: Oceans, 118(2), 619–634, doi: 10.1029/2012JC008306, 2013.

Revil-Baudard, T., J. Chauchat, D. Hurther, and P.-A. Bar- raud, Investigation of sheet-flow processes based on novel acoustic high-resolution velocity and concentration mea- surements, Journal of Fluid Mechanics, 767, 1–30, doi: 10.1017/jfm.2015.23, 2015.

Revil-Baudard, T., J. Chauchat, D. Hurther, and O. Eiff, Tur- bulence modifications induced by the bed mobility in intense sediment-laden flows, Journal of Fluid Mechanics, 808, 469– 484, doi:10.1017/jfm.2016.671, 2016.

Sumer, B. M., A. Kozakiewicz, J. Fredsøe, and R. Deigaard, Ve- locity and Concentration Profiles in Sheet-Flow Layer of Mov- able Bed, Journal of Hydraulic Engineering, 122 (10), 549–558, doi:10.1061/(ASCE)0733-9429(1996)122:10(549), 1996.

Thorne P.D. and Hurther D. 2014. An Overview on the use of backscattered sound for measuring suspended particle size and concentration profiles in non-cohesive inorganic sediment transport studies. Continental Shelf Research. 73, 97-118.

Thorne, P. D., and D. Hurther, An overview on the use of backscattered sound for measuring suspended particle size and concentration profiles in non-cohesive inorganic sediment transport studies, Continental Shelf Research, 73(0), 97–118, doi:10.1016/j.csr.2013.10.017, 2014.